Nanoscale

PAPER

View Article Online
View Journal | View Issue

Cite this: *Nanoscale*, 2024, **16**, 6522

Ruptured liquid metal microcapsules enabling hybridized silver nanowire networks towards high-performance deformable transparent conductors†

Shipeng Wang,‡[a] Huaisen Tian,‡[a] Yawen Wang,[b] Haojie Zuo,[b] Chengliang Tao,[a] Jiawei Liu,[a] Pengyuan Li,[a] Yan Yang,[a] Xu Kou,[a] Jiangxin Wang*[a] and Wenbin Kang *[b]

Received 20th December 2023,
Accepted 26th February 2024

DOI: 10.1039/d3nr06508a

rsc.li/nanoscale

Extensive studies have been carried out on silver nanowires (AgNWs) in view of their impressive conductivity and highly flexible one-dimensional structure. They are seen as a promising choice for producing deformable transparent conductors. Nonetheless, the widespread adoption of AgNW-based transparent conductors is hindered by critical challenges represented by the significant contact resistance at the nanowire junctions and inadequate interfacial adhesion between the nanowires and the substrate. This study presents a novel solution to tackle the aforementioned challenges by capitalizing on liquid metal microcapsules (LMMs). Upon exposure to acid vapor, the encapsulated LMMs rupture, releasing the fluid LM which then forms a metallic overlay and hybridizes with the underlying Ag network. As a result, a transparent conductive film with greatly enhanced electrical and mechanical properties was obtained. The transparent conductor displays negligible resistance variation even after undergoing chemical stability, adhesion, and bending tests, and ultrasonic treatment. This indicates its outstanding adhesion strength to the substrate and mechanical flexibility. The exceptional electrical properties and robust mechanical stability of the transparent conductor position it as an ideal choice for direct integration into flexible touch panels and wearable strain sensors, as evidenced in this study. By resolving the critical challenges in this field, the proposed strategy establishes a compelling roadmap to navigate the development of high-performance AgNW-based transparent conductors, setting a solid foundation for further advancement in the field of deformable electronics.

Introduction

Various conventional electronic devices including solar cells,[1–3] touch screens,[4,5] transparent heaters,[6,7] electromagnetic interference shielding,[8,9] light-emitting diodes (LEDs) and others[10,11] are being developed towards high deformability. Transparent conductors that possess excellent conductivity, high optical transmittance, and superior mechanical stability are essential for the advancement of these flexible electronic devices. Despite the dominance of Indium Tin Oxide (ITO) electrodes in the market for transparent conductors, their brittleness and the scarcity of indium constrain their extensive use in deformable electronic devices.[12] Currently, various functional materials are being investigated to substitute ITO, including metal grids,[13] carbon nanotubes,[14,15] graphene,[16,17] conducting polymers (PEDOT:PSS) and metal nanowires.[18–20] Among the various materials, silver nanowires (AgNWs) have attracted considerable interest due to their superior intrinsic conductivity and optical properties, well-established solution-based processing techniques, and notable mechanical flexibility.[21,22] Conductors based on silver nanowires have been used for various applications, including color changing soft robotics,[23,24] stretchable and transparent supercapacitors,[25,26] flexible sensors,[27,28] air filters and flexible fuel cells.[29–33] Despite the progress made, there are still significant challenges that need to be addressed in achieving high-performance transparent conductors using AgNWs. These challenges include the presence of high contact resistance, surface roughness, and inadequate adhesion between the conductive networks and the substrates.[34] The high contact resistance between silver nanowires is a result of the insulating surfactant coating of polyvinylpyrrolidone (PVP) and weak contact at the junctions. Various post-treatment techniques have been

---

[a] *School of Mechanical Engineering, Sichuan University, Chengdu 610065, China. E-mail: wangjiangxin@scu.edu.cn*

[b] *State Key Laboratory of Environment-Friendly Energy Materials, Southwest University of Science and Technology, Mianyang, 621010, China. E-mail: wenbin.kang@swust.edu.cn*

† Electronic supplementary information (ESI) available. See DOI: **https://doi.org/10.1039/d3nr06508a**

‡ These authors contributed equally to this manuscript.

proposed to tackle these issues, such as heat treatment,[35,36] mechanical pressing,[37] capillary-force-induced welding,[38,39] laser nano-welding,[40] chemical reactions,[41] nano-joining at the junctions with CNTs,[42] atomic layer deposition (ALD),[43] plasmonic treatment,[44] *etc*. However, these methods are characterized by complexity and high cost, requiring specialized conditions and equipment, as shown in Table S1.† For instance, heat treatment necessitates precise control over heat duration and temperature to prevent oxidation and fracture of AgNWs.[35] Mechanical pressing, when applied with excessive pressure, can impair the functional integrity of devices.[45] Capillary force can effectively weld silver nanowire junctions. However, in order to obtain the ideal welding effect, it is necessary to consider the viscosity coefficient of the solution and the volatility rate and other factors, which greatly increases the difficulty of the operation.[46] Similarly, laser nano-welding, ALD and plasmonic treatments require expensive, specialized equipment, posing obstacles for mass production. Moreover, after post-treatment with these methods, AgNW networks need to be transferred into flexible substrates, which cannot directly enhance the adhesion with the substrate. Furthermore, it is important to note that following post-treatment using these methods, the AgNW networks require transfer onto flexible substrates. This transfer process does not inherently improve the adhesion between the AgNW networks and the substrate. Therefore, a simple and effective approach to improve the performance of transparent conductors is in high demand to spur the development of deformable electronics.

Gallium-based liquid metals are an emerging class of conductive materials that possess both the high conductivity of metals and the fluidity of liquids.[47] Compared to conventional conductive materials, the unique properties of liquid metals with intrinsic conformability, excellent conductivity, and good biosafety make them highly attractive for applications in the field of deformable electronics. Liquid metals exhibit excellent wettability to rigid metals such as silver,[48] nickel,[49] and copper,[50] leading to irreversible bonding through the formation of an intermetallic-phase.[51,52] This characteristic allows liquid metals to provide both electrical robustness and mechanical conformity when welding metallic materials and achieving intermetallic bond-assisted LM patterning.[53,54] For example, a liquid metal micro/nanomotor has been developed to weld silver nanowire junctions at room temperature.[55] A novel liquid metal-based conductor of a LM and AgNW backbone has been developed to achieve direct patterning of the stretchable conductor. Through a laser-induced photothermal reaction, the oxide shell of the microcapsules ruptures and the liquid metal connects to the adjacent LM and silver nanowires.[56,57]

In this study, we present a post-treatment method for the AgNW network that utilizes a LM to effectively improve the performance of transparent conductors. Through acid treatment, the homogeneously distributed LMMs rupture to release the fluid LM that subsequently covers and hybridizes with the underlying AgNW network. This immediately remedies the sheet resistance and enhances the mechanical robustness of the transparent conductor. This transparent conductor exhibits outstanding adhesion to the substrate, making it suitable for direct application as a touch panel. It demonstrates stable operation even after undergoing a rigorous adhesion test with 3M VHB tape. Furthermore, the deformable transparent conductor, composed of AgNWs–LM, can be utilized as a wearable strain sensor to monitor various human movements, such as finger bending, wrist motions, feet gait, and throat swallowing.

Wenbin Kang

Wenbin Kang, after receiving his Ph.D. from Nanyang Technological University (2012–2017), became an Associate Professor at Sichuan University and later a Professor at Southwest University of Science and Technology. Recognized for his expertise in the field of materials science, he was recruited into the "Thousand Talent Program" of Sichuan Province in 2018. Kang specializes in additive manufacturing to enhance the performance of electrochemical energy storage devices, with a focus on revolutionizing traditional 2D devices through digital patterning. Additionally, he is actively engaged in the development of flexible devices such as intelligent displays and stretchable sensors to elevate human–machine interactions.

Experimental

Materials

Silver nanowires with diameters of ~50 nm and lengths of 100–150 μm were provided by Nanjing XFNANO Materials Technol. (China) in the suspension form in isopropyl alcohol (IPA) (concentration: 10 mg ml^{-1}, the molecular weight of PVP: 58 000). The gallium–indium alloy LM (gallium 75%/indium 25%) was purchased from Dongguan Huatai Metal Materials Technology Co., Ltd. IPA was provided by Macklin. HCl solution (36–38 wt%) was obtained from Chengdu Kelong Chemical Reagent Co., Ltd.

Preparation of LM microcapsules

The LM (60 mg) was dispersed in 20 ml of IPA and then sonicated at a power of 600 W for 20 minutes. After sonication, a grey suspension was obtained, which was subsequently further diluted to 1 mg ml^{-1} with IPA.

Characterization

The optical transmittance was characterized using a UV-visible spectrometer (UV-1900, UV-3600, Shimadzu). The sheet resistance was determined through a four-probe resistivity tester (HPS2662, Changzhou Helpass Electronic Technology Reagent

Co., Ltd). The microstructure of the samples was examined by using scanning electron microscopy (SEM, JSM7500F, Japan). The cyclic bending test on the transparent conductor was carried out on a single arm universal testing system (JHY-5000, Suzhou Xingsuo Intelligent Device Reagent Co., Ltd).

Results and discussion

A schematic depicting the workflow to obtain the AgNW–LM conductor is shown in Fig. 1a. Initially, these suspensions were prepared at a concentration of 0.5 mg ml^{-1}, with volumes ranging from 0.25 to 0.5 ml, and sprayed to the substrate measuring 25 × 25 mm^2 (glass, PET, or TPU). The application of increased quantities of AgNWs inversely affected both the sheet resistance and transmittance of the resulting transparent conductors. Then, 0.25 ml of LMM suspension was applied onto the Ag NW network. The substrate was eventually inverted and positioned 1 cm above the Petri dish filled with HCl solution (36–38 wt%). The substrates treated with HCl vapor were subsequently dried in a controlled drying oven at 35 °C for 4 hours to effectively remove any residual moisture and HCl from the substrate's surface. SEM images confirm the transformation of LMMs into a thin metallic film that covers the silver nanowires following HCl vapor treatment. As illustrated in Fig. 1b and c, LMMs of varying sizes (1–2 μm) were present on the surface of the AgNW networks before HCl vapor treatment. An oxide layer is present on the surface of LMMs, which stabilizes them in solution and facilitates their uniform dispersion onto substrates *via* spray-coating. Upon exposure of the substrate containing AgNWs and LMMs to HCl vapor, the $\mathrm{Ga_2O_3}$ oxide layer on LMMs, typically 2–3 nm thick, is swiftly eliminated.[58] The LMMs correspondingly rupture, releasing the fluid LM to involve in reactive wetting by forming metallic bonds with the percolating AgNWs underneath. Finally, a hybridized conductive network was constructed as shown in Fig. 1d–f. The thickness of the liquid metal film is around 0.3–0.4 μm, as shown in Fig. S1.† The Energy-Dispersive X-ray Spectroscopy (EDS) pattern (Fig. 1g) further validates the existence of gallium, indium, and silver in the hybridized conductor. As shown in Fig. S2,† when without LMMs, silver nanowires react with HCl to generate insulating silver chloride aggregates, which ultimately lead to the fracture of the silver nanowires, causing an increase in the sheet resistance of the

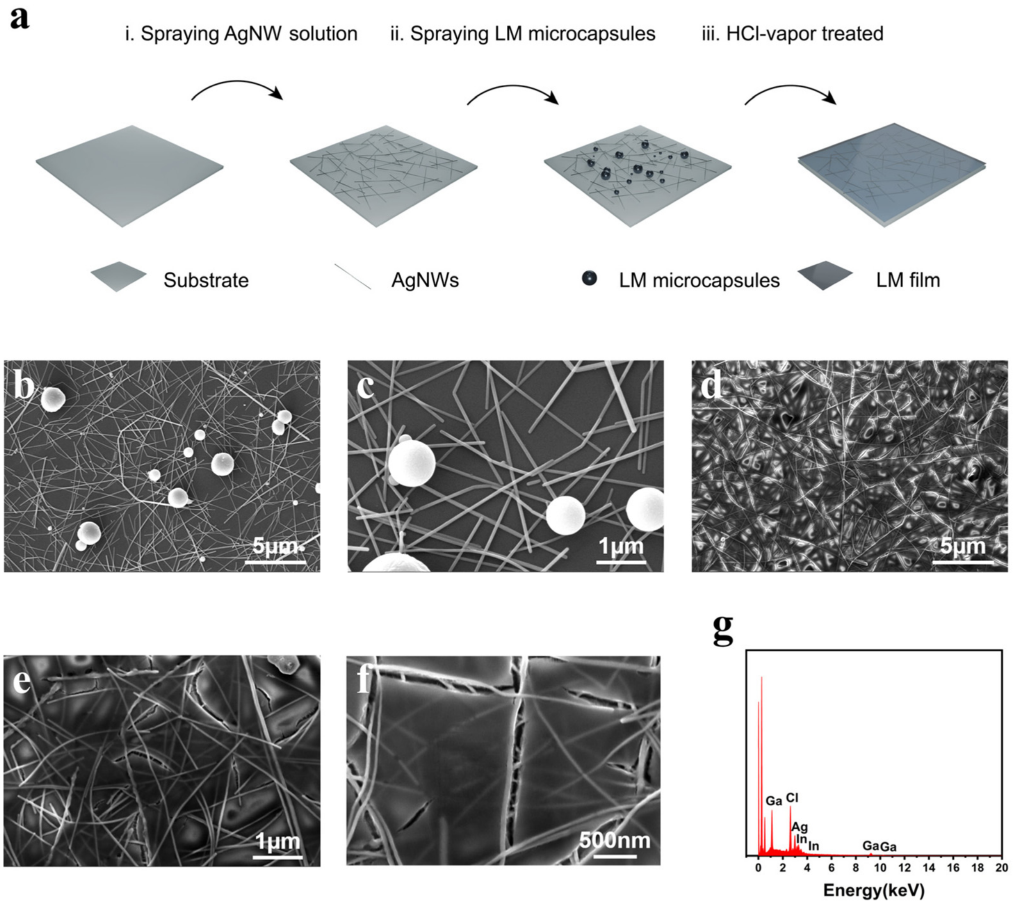

Fig. 1 (a) Schematic illustrating the process to obtain transparent AgNW–LM conductors. (b and c) SEM images of the transparent conductor before HCl vapor treatment. (d–f) SEM images of the transparent conductor after HCl vapor treatment. (g) EDS pattern of the hybrid conductor on the substrate.

conductive network. In addition, the incorporation of Ag is crucial in addressing the inherent high surface tension characteristic of LM. This strategic integration of Ag enables reactive wetting with LM, facilitating its seamless integration onto target substrates. In the absence of Ag, LM tends to demonstrate poor wetting properties, leading to its coalescence into larger microcapsules rather than forming a uniform layer on the substrates (Fig. S3†).

Fig. 2a illustrates the impact of spayed LMMs and HCl vapor-induced microcapsule rupture on optical transmittance and sheet resistance. After spraying LMMs, both the optical transmittance and sheet resistance of the conducting films decrease. As shown in Fig. S4,† the transmittance decreases while the haze increases due to the presence of LMMs, which act as scattering centers and impede the transmission of light. The LMMs are weakly connected with adjacent silver nanowires through physical adsorption. After HCl vapor treatment, the LMMs transform into a metallic film covering the AgNW networks. The sheet resistance of the conductor is significantly improved through the welding of the inter-wire junction by the LM during this process. This reduces contact resistance and creates an additional conducting pathway through the metallic film. Fig. 2b shows the transmittance spectra of typical AgNWs–LM conductors of different sheet resistances on the PET substrate. The transparent conductor, with a sheet resistance of 13.00 Ω sq^{-1}, delivers a transmittance of 78% at 550 nm; by comparison, the electrode exhibiting a slightly larger sheet resistance of 17.58 Ω sq^{-1} shows an improved transmittance of 80% at 550 nm. Moreover, as shown in Fig. S5,† the sheet resistance and transmittance in the central

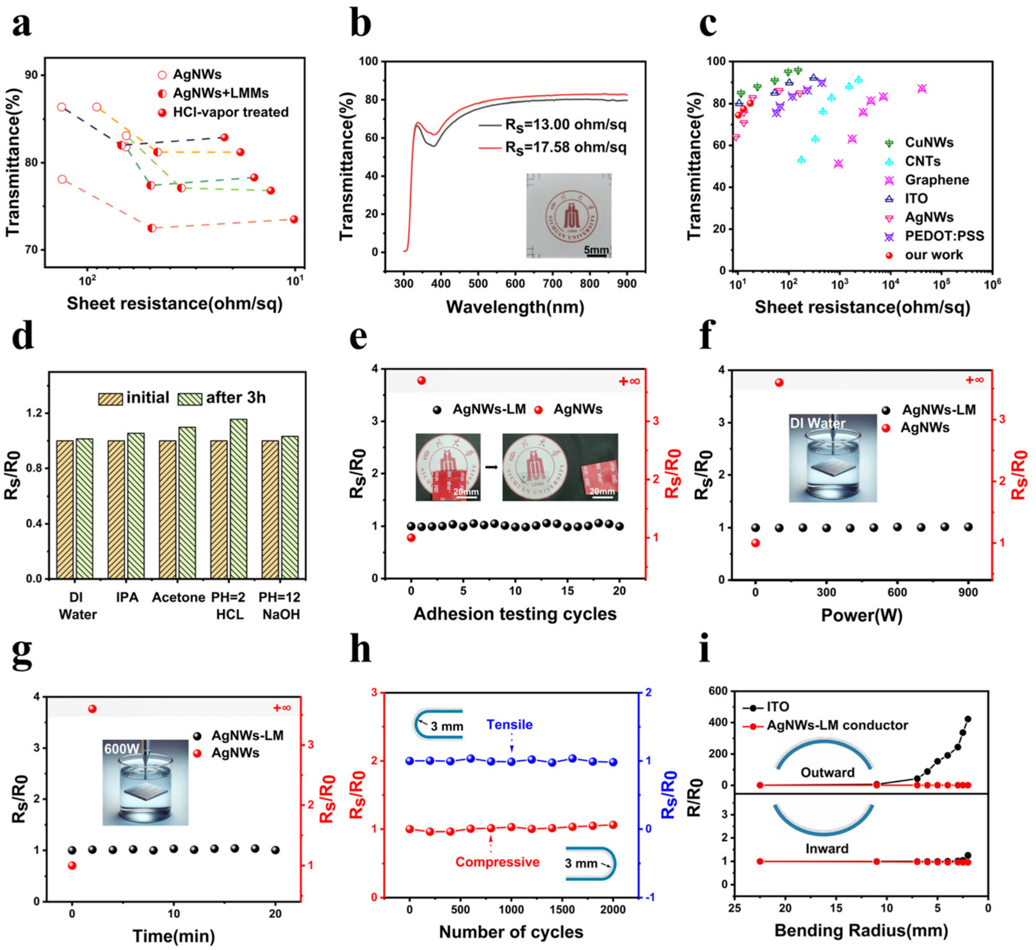

Fig. 2 (a) The impact of spayed LMMs and HCl vapor-induced microcapsule rupture on optical transmittance (UV-1900, with the transmittance of the substrate subtracted) and sheet resistance. (b) The transmittance spectra of the AgNW–LM conductor of different sheet resistances on the PET substrate (UV-3600, using the integrating sphere with the reference of bare air). (c) The electro-optical performance of the AgNW–LM transparent conductor compared with reported works based on ITO, PEDOT:PSS, graphene, CNTs, AgNWs, and CuNWs. (d) The sheet resistance variation of the AgNW–LM conductor after immersion in various solvents, including DI water, IPA, acetone, acidic (HCl, pH = 2.0), and alkaline (NaOH, pH = 12.0) solution. (e) Variation in sheet resistance following cyclic adhesion tests with 3M VHB tape on the AgNW–LM conductor. (f) The sheet resistance variation of the AgNW–LM conductor after 60 seconds of ultrasonic treatment at varying power levels in DI water. (g) The sheet resistance variation of the AgNW–LM conductor under 600 W ultrasonic treatment in DI water for 20 min. (h) Analysis of the sheet resistance variation of the AgNW–LM conductor in tensile and compressive modes with a bending radius of 3 mm. (i) Inward and outward bending tests on the AgNW–LM conductor and ITO films at a gradually reduced bending radius.

region of the transparent conductor did not significantly differ from those at the edge, which suggests the excellent uniformity of the electrode in terms of electrical and optical properties. A representative AgNW–LM conductor is able to deliver 10.23 Ω sq^{-1} at $T = 75\%$, 13.00 Ω sq^{-1} at $T = 78\%$, and 17.58 Ω sq^{-1} at $T = 80\%$ (Fig. 2c), which are on par with ITO and surpass the majority of previously reported transparent conductors including CNTs,[59] graphene,[60] PEDOT:PSS,[61] AgNWs, and CuNWs.[62,63]

Achieving chemical stability and mechanical robustness is essential for the practical use of transparent conductors in deformable electronic devices. However, this is challenging with exposed AgNWs, which are susceptible to damage in open environments. The formation of a metallic overlay from LMM rupture results in significantly improved stability of the transparent conductors under harsh conditions. As shown in Fig. 2d, the sheet resistance of the transparent conductor remains virtually unchanged even after 3 h of immersion in different solvents, including deionized (DI) water, IPA, acetone, acidic solution (pH = 2.0), and alkaline solution (pH = 12.0). Remarkably, this stability extends to highly corrosive environments, such as a concentrated HCl vapor environment, underscoring the conductor's robustness under diverse chemical conditions, as shown in Fig. S6.† In addition, due to the protection of the LM film, the transparent conductor exhibits stable conductivity after 12 days of exposure to air ($R_s/R_0 < 1.3$), whereas the nanowires on the substrate surface are rapidly oxidized ($R_s/R_0 > 9$), as shown in Fig. S7.† To further investigate the mechanical robustness of the AgNW–LM conductor, adhesion test, ultrasonic treatment and cyclic bending tests were performed. The sheet resistance of the samples used for testing is listed in Table S2 of the ESI.† The sheet resistance of the AgNW–LM conductor remains stable even after undergoing 20 adhesion tests with 3M VHB tape (3M VHB tape 4910), as depicted in Fig. 2e. The SEM images depicting the electrode morphology before and after the adhesion test are presented in Fig. S8.† Following the adhesive testing, the liquid metal film remains intact over the Ag NWs, while the silver nanowires on the substrate surface become detached in the absence of the LM film's protection. Moreover, the sheet resistance of the AgNW–LM conductor shows minimal variation following ultrasonic treatment at different power levels for 60 seconds and at 600 W for 20 minutes, both in DI water and IPA solution, as demonstrated in Fig. 2f, g and Fig. S9, S10.† By comparison, the sheet resistance of the AgNW conductor exceeds the measurement range of our instrument (>2 MΩ) after undergoing the first adhesion test and ultrasonic treatment. These test results indicate that the LM film significantly enhances the adhesion strength of the AgNW network to the substrate. Compressive and tensile bending tests were also conducted using a bending stage. As shown in Fig. 2h, the transparent conductor maintains its sheet resistance nearly unchanged even after undergoing 2000 bending cycles with a 3 mm bending radius. Unlike commercial ITO electrodes that are limited by their inherent brittleness, the transparent AgNW–LM conductor demonstrates remarkable mechanical stability. As shown in Fig. 2i, the resistance of the AgNW–LM

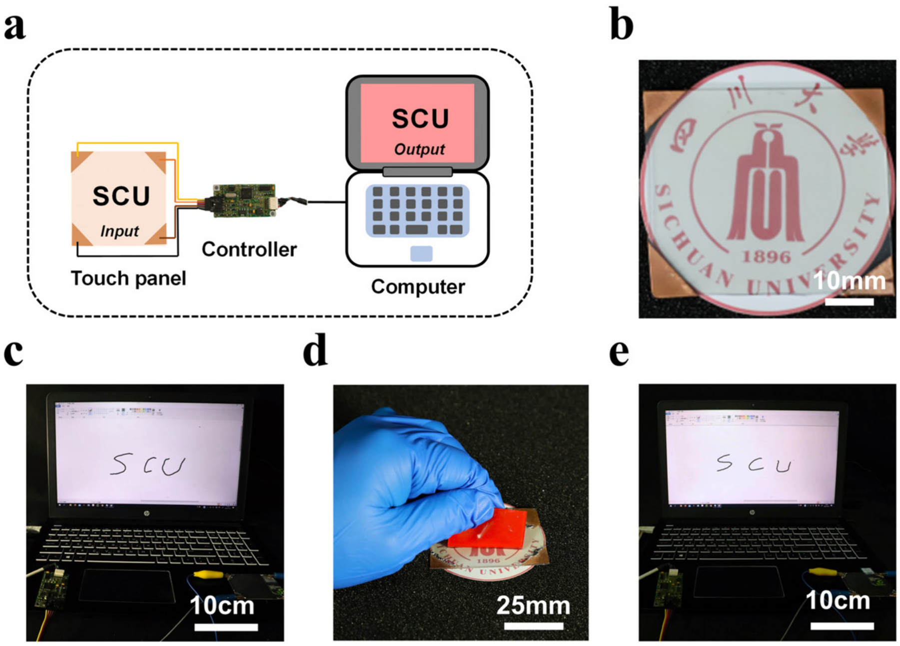

Fig. 3 (a) Schematic illustrating the components of the touch system, including the touch panel, controller and computer. (b) Digital image of the touch panel (50 × 40 mm^2) based on the AgNW–LM transparent conductor. (c) Touch panel function showcased through the writing of the letters "SCU". (d) Image of the touch panel being subjected to adhesion test with 3M VHB tape. (e) Confirmation of the operation stability of the touch panel by reflecting "SCU" letters on the screen after the adhesion test.

conductor remains nearly constant as the bending radius gradually decreases, regardless of inward or outward bending tests. In contrast, the conductivity of the commercial ITO-coated PET (ITO/PET) conductor significantly decreases during outward bending. To visually demonstrate the improved mechanical stability, LED lights were connected to the ITO and AgNW–LM conductors, as depicted in Fig. S11.† Following the bending test, the brightness of the LED significantly decreases as a result of the elevated resistance in the ITO electrode. Conversely, the AgNW–LM electrode maintains a consistent conductivity, ensuring stable light emission. The changes in the resistance of the ITO/PET electrode and AgNW–LM/TPU electrode under stretching are shown in Fig. S12–S14.† The ITO/PET electrode lost its conductivity at a strain of 7%, while the AgNW–LM conductor remains highly conductive even at a strain of 50%. The results suggest that constructing a metallic overlay that hybridizes with the AgNW networks from ruptured LMMs is an effective approach for achieving high-performance transparent conductors. The LM film reduces the contact resistance between the silver nanowires while protecting the AgNW networks against damage. It also enhances the adhesion of the conductive layer to the substrate, resulting in excellent mechanical reliability of the transparent conductor. In addition, this method is further applied to copper nanowire (CuNW) networks, as shown in Fig. S15.† After HCl vapor treatment, the LM reactively wets the underlying CuNWs, forming a hybridized electrode, and the sheet resistance of the CuNW–LM electrode is decreased significantly. Therefore, the method presented in this study possesses broad applicability and potential for adaptation to other metallic systems beyond silver.

The exceptional mechanical stability and high conductivity of the transparent conductor make it highly suitable for a wide range of deformable optoelectronic devices.[64] For instance, a touch sensing device is an important application that utilizes transparent conductive materials. In this case, a surface capacitive touch panel based on the AgNW–LM conductor is presented. Fig. 3a schematically illustrates the operation of the

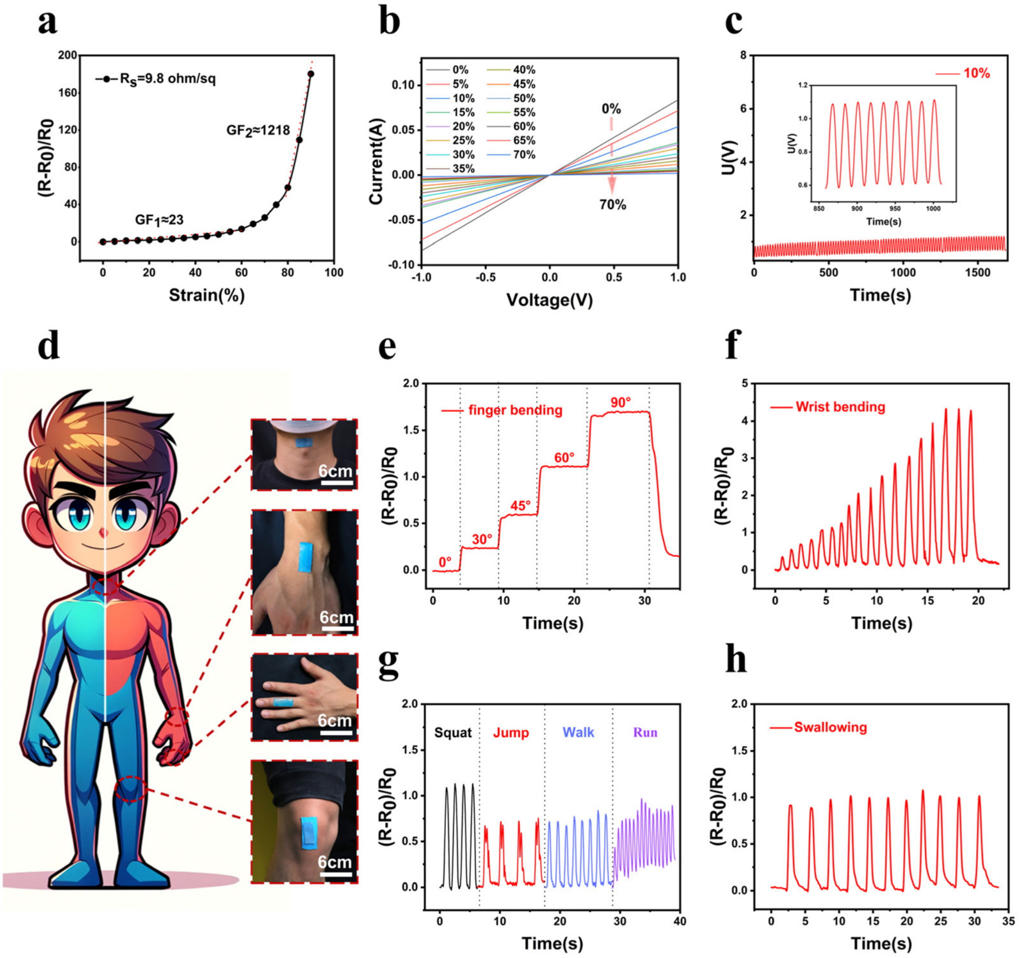

Fig. 4 (a) Gauge factor of the deformable strain sensor with a sheet resistance of 9.8 Ω sq^{-1}. (b) Current–voltage (*I*–*V*) curve of the strain sensor under varying applied strains. (c) Change in resistance of the strain sensor in 100 loading–unloading cycles at 10% strain. Inset: a magnified view of the resistance during loading and unloading. (d) Schematic figure illustrating the sensor being attached to different parts of the human body. Response curves for the detection of human body motion: (e) finger bending; (f) wrist bending; (g) gait behaviors; and (h) swallowing.

touch sensing system. The system includes the touch panel fabricated with the AgNW–LM conductor, an electrical board to detect the capacitance change in the touch panel, and a computer to display the touch signal. A digital image showcasing the touch panel is presented in Fig. 3b. A copper film was employed to establish a connection between the touch panel and the external controller, and the interface between the copper film and the transparent conductive layer was further improved using the LM. The input figures on the touch panel were effectively displayed on the computer *via* the integrated controller, as illustrated in Fig. 3c. Notably, the touch panel maintains its sensing capabilities even after undergoing the adhesion test with 3M VHB tape, as shown in Fig. 3d and e. The touch signal was consistently captured and displayed on the monitor, even after 10 repetitions of the peeling test. The observation illustrates the effective protection provided by the LM overlay to the percolating AgNWs, resulting in a substantial improvement in the adhesion stability of the hybrid conductor.

Strain sensors capable of conforming to human skin play a crucial role in gathering biophysical data for human motion detection, healthcare monitoring, and human–computer interactions. The AgNW–LM transparent conductor serves effectively as a strain sensor, owing to its excellent mechanical compliance and strong adhesion of the conductive layer to the substrate. Fig. 4a displays the gauge factor (GF) of the strain sensor made with AgNWs–LM coated on thermoplastic polyurethane (TPU), capable of stretching up to 550% strain (Fig. S14†). The strain sensor, with a sheet resistance of 9.8 Ω sq^{-1}, operates within a strain range of 0–95%, exhibiting a lower GF of 23 in the 0–60% strain range and a higher GF of 1218 in the 60–95% range. Fig. 4b shows the current–voltage (*I*–*V*) curves of the strain sensor at different tensile strains. As the voltage gradually increases, the current exhibits a linear increase. The *I*–*V* curve consistently demonstrates ohmic behavior within the 0–70% strain range. Durability is a key performance indicator for strain sensors in practical applications. Fig. 4c shows that the AgNW–LM sensor maintains excellent stability and repeatability over 100 loading and unloading cycles at a strain of 10%. Fig. 4d demonstrates the sensor's ability to attach to various parts of the human body for motion detection with kinesiology tape and thin VHB tape (as shown in Fig. S16†). Fig. 4e shows the change in resistance when the sensor is adhered to a human finger. The change in relative resistance accurately indicates the extent of finger bending. Additionally, the sensor can be affixed to the wrist or knee joint, providing high-quality measurements of individual physical activities. As depicted in Fig. 4f, the monitored resistance signal correlates with the frequency and amplitude of wrist bending. The strain sensor's excellent conformability and sensitivity enable it to monitor real-time knee joint motions. Different knee-related movements, such as squatting, jumping, walking, and running, can be easily identified through the variations in the resistance signal, as shown in Fig. 4g. Besides tracking large-scale human movements, the sensor is also capable of detecting subtle body movements. As illustrated in Fig. 4h, when the sensor is attached to a volunteer's neck, it can detect glottal movements during swallowing.

Conclusions

In conclusion, this study proposes a straightforward yet highly efficacious method for creating high-performance, deformable transparent conductors with versatile functionality, leveraging the unique physicochemical properties of LM. When subjected to acid vapor, the enclosed liquid metal microcapsules rupture, releasing the fluid metal. The liberated metal subsequently forms a metallic overlay and hybridizes with the underlying Ag network, yielding a transparent conductive film with significantly improved electrical and mechanical properties. A transparent conductor with a sheet resistance of 15.27 Ω sq^{-1} and an optical transmittance of 81% at 550 nm was successfully fabricated on a PET substrate. Significantly, the AgNW–LM conductor demonstrated outstanding deformability and reliability, enduring a series of rigorous stability tests such as chemical stability, adhesion tests (with 3M VHB tape), ultrasonic treatment, and 2000 cycles of compressive and tensile bending. The versatile functionality of the transparent conductor was demonstrated through its integration into touch panels and strain sensors. The exceptional performance and stable operation of the assembled devices highlight the effectiveness of the hybrid deformable electrode design and its potential for driving innovations in advanced deformable electronics.

Conflicts of interest

There are no conflicts to declare.

Acknowledgements

This work was supported by the Excellent Youth in Science and Technology Program of Sichuan Province, China (Grant No. 2022JDJQ0028), the Research Startup Funding by Sichuan University, China (Grant No. YJ202218), and the Longshan Academic Talent Research Supporting Program of SWUST (no. 22zx7102).

References

1 X. Chen, G. Xu, G. Zeng, H. Gu, H. Chen, H. Xu, H. Yao, Y. Li, J. Hou and Y. Li, *Adv. Mater.*, 2020, **32**, 1908478.

2 R. E. Booth, H. M. Schrickx, G. Hanby, Y. Liu, Y. Qin, H. Ade, Y. Zhu and B. T. O'Connor, *Sol. RRL*, 2022, 2200264.

3 Y. Zhang, S. Ng, X. Lu and Z. Zheng, *Chem. Rev.*, 2020, **120**, 2049–2122.

4 J. Xiong, S. Li, Y. Ye, J. Wang, K. Qian, P. Cui, D. Gao, M. Lin, T. Chen and P. S. Lee, *Adv. Mater.*, 2018, **30**, 1802803.

5 B. Han, K. Pei, Y. Huang, X. Zhang, Q. Rong, Q. Lin, Y. Guo, T. Sun, C. Guo, D. Carnahan, M. Giersig, Y. Wang, J. Gao, Z. Ren and K. Kempa, *Adv. Mater.*, 2014, **26**, 873–877.

6 W. Lan, Y. Chen, Z. Yang, W. Han, J. Zhou, Y. Zhang, J. Wang, G. Tang, Y. Wei, W. Dou, Q. Su and E. Xie, *ACS Appl. Mater. Interfaces*, 2017, **9**, 6644–6651.

7 B. Sun, R. Xu, X. Han, J. Xu, W. Hong, Y. Xu, Z. Fu, H. Zhu, X. Sun, J. Wang, P. Cui, J. Chang, J. Xiong and K. Qian, *npj Flexible Electron.*, 2022, **6**, 1–9.

8 M. Jin, W. Chen, L. Liu, H. Zhang, L. Ye, P. Min and Z. Yu, *J. Mater. Chem. A*, 2022, **10**, 14364–14373.

9 N. Zhang, Z. Wang, R. Song, Q. Wang, H. Chen, B. Zhang, H. Lv, Z. Wu and D. He, *Sci. Bull.*, 2019, **64**, 540–546.

10 S. Kim and B. Hwang, *Mater. Des.*, 2018, **160**, 572–577.

11 K. Lee, J. Shin, J. Park, J. Lee, C. W. Joo, J. Lee, D. Cho, J. T. Lim, M. Oh, B. Ju and J. Moon, *ACS Appl. Mater. Interfaces*, 2016, **8**, 17409–17415.

12 M. Lee, Y. Jo, D. S. Kim, H. Y. Jeong and Y. Jun, *J. Mater. Chem. A*, 2015, **3**, 14592–14597.

13 J. Kang, C. G. Park, S. H. Lee, C. Cho, D. G. Choi and J. Y. Lee, *Nanoscale*, 2016, **8**, 11217–11223.

14 L. Cai, J. Li, P. Luan, H. Dong, D. Zhao, Q. Zhang, X. Zhang, M. Tu, Q. Zeng, W. Zhou and S. Xie, *Adv. Funct. Mater.*, 2012, **22**, 5238–5244.

15 S. S. Siwal, A. K. Saini, S. Rarotra, Q. Zhang and V. K. Thakur, *J. Nanostruct. Chem.*, 2021, **11**, 93–130.

16 N. Li, S. Oida, G. S. Tulevski, S. Han, J. B. Hannon, D. K. Sadana and T. Chen, *Nat. Commun.*, 2013, **4**, 2294.

17 T. Chen, Y. Xue, A. K. Roy and L. Dai, *ACS Nano*, 2014, **8**, 1039–1046.

18 J. H. Lee, Y. R. Jeong, G. Lee, S. W. Jin, Y. H. Lee, S. Y. Hong, H. Park, J. W. Kim, S. Lee and J. S. Ha, *ACS Appl. Mater. Interfaces*, 2018, **10**, 28027–28035.

19 L. V. Kayser and D. J. Lipomi, *Adv. Mater.*, 2019, **31**, 1806133.

20 S. Ye, A. R. Rathmell, Z. Chen, I. E. Stewart and B. J. Wiley, *Adv. Mater.*, 2014, **26**, 6670–6687.

21 Y. Chen, R. S. Carmichael and T. B. Carmichael, *ACS Appl. Mater. Interfaces*, 2019, **11**, 31210–31219.

22 Z. He, J. Wang, S. Chen, J. Liu and S. Yu, *Acc. Chem. Res.*, 2022, **55**, 1480–1491.

23 P. Won, K. K. Kim, H. Kim, J. J. Park, I. Ha, J. Shin, J. Jung, H. Cho, J. Kwon, H. Lee and S. H. Ko, *Adv. Mater.*, 2021, **33**, 2002397.

24 H. Kim, S. Ahn, D. M. Mackie, J. Kwon, S. H. Kim, C. Choi, Y. H. Moon, H. B. Lee and S. H. Ko, *Mater. Today*, 2020, **41**, 243–269.

25 H. Kim, K. R. Pyun, M. T. Lee, H. B. Lee and S. H. Ko, *Adv. Funct. Mater.*, 2022, **32**, 2110535.

26 J. Jung, H. Cho, R. Yuksel, D. Kim, H. Lee, J. Kwon, P. Lee, J. Yeo, S. Hong, H. E. Unalan, S. Han and S. H. Ko, *Nanoscale*, 2019, **11**, 20356–20378.

27 H. Jeong, Y. Noh, S. H. Ko and D. Lee, *Compos. Sci. Technol.*, 2019, **174**, 50–57.

28 P. Won, J. J. Park, T. Lee, I. Ha, S. Han, M. Choi, J. Lee, S. Hong, K. Cho and S. H. Ko, *Nano Lett.*, 2019, **19**, 6087–6096.

29 K. Park, S. Kang, J. Park and J. Hwang, *J. Hazard. Mater.*, 2021, **411**, 125043.

30 S. Jeong, H. Cho, S. Han, P. Won, H. Lee, S. Hong, J. Yeo, J. Kwon and S. H. Ko, *Nano Lett.*, 2017, **17**, 4339–4346.

31 I. Chang, T. Park, J. Lee, H. B. Lee, S. Ji, M. H. Lee, S. H. Ko and S. W. Cha, *Int. J. Hydrogen Energy*, 2014, **39**, 7422–7427.

32 T. Park, I. Chang, H. B. Lee, S. H. Ko and S. W. Cha, *Int. J. Hydrogen Energy*, 2017, **42**, 1884–1890.

33 I. Chang, T. Park, J. Lee, M. H. Lee, S. H. Ko and S. W. Cha, *J. Mater. Chem. A*, 2013, **1**, 8541.

34 D. S. Hecht, L. Hu and G. Irvin, *Adv. Mater.*, 2011, **23**, 1482–1513.

35 Z. Cui, F. R. Poblete and Y. Zhu, *ACS Appl. Mater. Interfaces*, 2019, **11**, 17836–17842.

36 T. Song, Y. Chen, C. Chung, Y. M. Yang, B. Bob, H. Duan, G. Li, K. Tu, Y. Huang and Y. Yang, *ACS Nano*, 2014, **8**, 2804–2811.

37 T. Tokuno, M. Nogi, M. Karakawa, J. Jiu, T. T. Nge, Y. Aso and K. Suganuma, *Nano Res.*, 2011, **4**, 1215–1222.

38 Y. Liu, J. Zhang, H. Gao, Y. Wang, Q. Liu, S. Huang, C. F. Guo and Z. Ren, *Nano Lett.*, 2017, **17**, 1090–1096.

39 K. Zhang, J. Li, Y. Fang, B. Luo, Y. Zhang, Y. Li, J. Zhou and B. Hu, *Nanoscale*, 2018, **10**, 12981–12990.

40 J. Lee, P. Lee, H. Lee, D. Lee, S. S. Lee and S. H. Ko, *Nanoscale*, 2012, **4**, 6408.

41 H. Lu, D. Zhang, J. Cheng, J. Liu, J. Mao and W. C. H. Choy, *Adv. Funct. Mater.*, 2015, **25**, 4211–4218.

42 P. Lee, J. Ham, J. Lee, S. Hong, S. Han, Y. D. Suh, S. E. Lee, J. Yeo, S. S. Lee, D. Lee and S. H. Ko, *Adv. Funct. Mater.*, 2014, **24**, 5671–5678.

43 D. Chen, J. Liang, C. Liu, G. Saldanha, F. Zhao, K. Tong, J. Liu and Q. Pei, *Adv. Funct. Mater.*, 2015, **25**, 7512–7520.

44 J. H. Park, G. Hwang, S. Kim, J. Seo, H. Park, K. Yu, T. Kim and K. J. Lee, *Adv. Mater.*, 2017, **29**, 1603473.

45 J. Tseng, L. Lee, Y. Huang, J. Chang, T. Su, Y. Shih, H. Lin and Y. Chueh, *Small*, 2018, **14**, 1800541.

46 C. Ma, Y. F. Liu, Y. G. Bi, X. L. Zhang, D. Yin, J. Feng and H. B. Sun, *Nanoscale*, 2021, **13**, 12423–12437.

47 M. D. Dickey, *Adv. Mater.*, 2017, **29**, 1606425.

48 M. Tavakoli, M. H. Malakooti, H. Paisana, Y. Ohm, D. Green Marques, P. Alhais Lopes, A. P. Piedade, A. T. Almeida and C. Majidi, *Adv. Mater.*, 2018, **30**, 1801852.

49 H. Chang, R. Guo, Z. Sun, H. Wang, Y. Hou, Q. Wang, W. Rao and J. Liu, *Adv. Mater. Interfaces*, 2018, **5**, 1800571.

50 M. I. Ralphs, N. Kemme, P. B. Vartak, E. Joseph, S. Tipnis, S. Turnage, K. N. Solanki, R. Y. Wang and K. Rykaczewski, *ACS Appl. Mater. Interfaces*, 2018, **10**, 2083–2092.

51 Y. Wang, H. Chang and W. Rao, *ACS Appl. Mater. Interfaces*, 2023, **15**, 24003–24012.

52 J. Tang, X. Zhao, J. Li, Y. Zhou and J. Liu, *Adv. Sci.*, 2017, **4**, 1700024.

53 R. Guo, H. Wang, G. Chen, B. Yuan, Y. Zhang and J. Liu, *Appl. Mater. Today*, 2020, **20**, 100738.

54 M. Kim, H. Lim and S. H. Ko, *Adv. Sci.*, 2023, **10**, 2205795.

55 Y. Wang, W. Duan, C. Zhou, Q. Liu, J. Gu, H. Ye, M. Li, W. Wang and X. Ma, *Adv. Mater.*, 2019, **31**, 1905067.

56 C. Cho, W. Shin, M. Kim, J. Bang, P. Won, S. Hong and S. H. Ko, *Small*, 2022, **18**, 2202841.

57 M. Kim, C. Cho, W. Shin, J. J. Park, J. Kim, P. Won, C. Majidi and S. H. Ko, *npj Flexible Electron.*, 2022, **6**, 98–99.

58 Y. Lin, C. Cooper, M. Wang, J. J. Adams, J. Genzer and M. D. Dickey, *Small*, 2015, **11**, 6397–6403.

59 A. A. Green and M. C. Hersam, *Nano Lett.*, 2008, **8**, 1417–1422.

60 A. A. Green and M. C. Hersam, *Nano Lett.*, 2009, **9**, 4031–4036.

61 Y. H. Kim, C. Sachse, M. L. Machala, C. May, L. Müller-Meskamp and K. Leo, *Adv. Funct. Mater.*, 2011, **21**, 1076–1081.

62 H. Wu, D. Kong, Z. Ruan, P. Hsu, S. Wang, Z. Yu, T. J. Carney, L. Hu, S. Fan and Y. Cui, *Nat. Nanotechnol.*, 2013, **8**, 421–425.

63 K. Ellmer, *Nat. Photonics*, 2012, **6**, 809–817.

64 M. Malischewski, M. Adelhardt, J. Sutter, K. Meyer and K. Seppelt, *Science*, 2016, **353**, 678–682.